

PAPER

View Article Online
View Journal

Cite this: DOI: 10.1039/d0ee02958k

Predicting the photocurrent–composition dependence in organic solar cells†

Xabier Rodríguez-Martínez,^a Enrique Pascual-San-José,^a Zhuping Fei,^b Martin Heeney,^b Roger Guimerà^{cd} and Mariano Campoy-Quiles^{*,a}

The continuous development of improved non-fullerene acceptors and deeper knowledge of the fundamental mechanisms governing performance underpin the vertiginous increase in efficiency witnessed by organic photovoltaics. While the influence of parameters like film thickness and morphology are generally understood, what determines the strong dependence of the photocurrent on the donor and acceptor fractions remains elusive. Here we approach this problem by training artificial intelligence algorithms with self-consistent datasets consisting of thousands of data points obtained by high-throughput evaluation methods. Two ensemble learning methods are implemented, namely a Bayesian machine scientist and a random decision forest. While the former demonstrates large descriptive power to complement the experimental high-throughput screening, the latter is found to predict with excellent accuracy the photocurrent–composition phase space for material systems outside the training set. Interestingly, we identify highly predictive models that only employ the materials band gaps, thus largely simplifying the rationale of the photocurrent–composition space.

Received 14th September 2020,
Accepted 5th January 2021

DOI: 10.1039/d0ee02958k

rsc.li/ees

Broader context

Multicomponent systems underline the significant performance improvements recently witnessed in many energy fields, from electrodes in batteries, to multication perovskites for photovoltaics and to high-ZT thermoelectric composites. Predicting the specific composition that would result in optimum performance is, however, one of the greatest unresolved problems in materials science. This is, in part, due to the fact that performance maximization is a complex multiparametric problem. Here we show that combining high-throughput experimental data with artificial intelligence (AI) algorithms enables unprecedented predicting capability. Specifically, we applied our methodology to the case of organic photovoltaics (OPV), since active layer composition is the parameter that affects more strongly OPV efficiency (e.g. 1:0 or 0:1 compositions result in zero efficiency for a blend whose optimum gives 18%). We generate thousands of data points in the performance–composition phase space for 15 different donor:acceptor blends and use the generated datasets to feed AI algorithms. Our work results in the identification of highly accurate and predictive models for the photocurrent–composition dependence unravelling the key material descriptors governing such behaviour (*i.e.* band gaps and charge mobility imbalance). This study paves the way for the use of AI and high-throughput experimentation to predict optimum composition in energy materials.

Introduction

The synthesis of novel conjugated semiconductors underpins the striking performance upswing that the field of organic photovoltaics (OPV) is currently experiencing.¹ Photoactive

blends of non-fullerene acceptors^{2–4} (NFAs) and low band gap donor co-polymers^{5,6} have demonstrated power conversion efficiencies (PCEs) over 18% in single-junction binary devices.⁷ Such figures result from an improved understanding of the donor:acceptor (D:A) material requirements in terms of extended light absorption, frontier energy level alignment and film morphology,^{8,9} as well as from enhanced charge transport properties.¹⁰ Indeed, the advanced understanding of many of the fundamental working principles in OPV combined with the inherent synthetic flexibility of conjugated materials is prompting the large-scale screening of potentially high-performing OPV material candidates. Yet, for a given material system, what could we say *a priori* about its OPV potential?

At the molecular level, computational algorithms such as those developed in the on-going Harvard Clean Energy Project

^a Institut de Ciència de Materials de Barcelona, ICMA-B-CSIC, Campus UAB, 08193, Bellaterra, Spain. E-mail: m.campoy@csic.es

^b Department of Chemistry and Centre for Plastic Electronics, White City Campus, Imperial College London, London W12 0BZ, UK

^c Institució Catalana de Recerca i Estudis Avançats, ICREA, Passeig de Lluís Companys 23, 08010, Barcelona, Spain

^d Department of Chemical Engineering, Universitat Rovira i Virgili, 43007, Tarragona, Spain

† Electronic supplementary information (ESI) available. See DOI: 10.1039/d0ee02958k



(CEP)¹¹ serve to rapidly pre-screen millions of molecular motifs and classify them according to their theoretical OPV outcome, thus motivating their ulterior synthesis. Beyond purely *in silico* screening, the development of data-driven models in the OPV field has so far been mostly restricted to data mining and training of artificial intelligence (AI) algorithms using intrinsic material descriptors.¹² This approach has been applied to make predictions in terms of novel materials^{13,14} and their corresponding expected PCE,¹⁵ as well as to guide researchers in the design of potentially top-performing materials.¹⁶ While promising, these calculations have had modest success thus far. This is due, in part, to the lack of sufficiently reproducible data in the literature; also to the difficulty to predict solid-state properties of the blend such as microstructure or gas-to-solid shifts in the optical properties and molecular energy levels; and finally, due to the fact that relevant device information is not considered in the calculations.¹⁷

At the device level, one aspect that has been modelled very successfully is the dependence of the performance on the active layer thickness. Device modelling based on transfer matrices has been demonstrated to reproduce accurately the mild oscillations of the photocurrent found experimentally.^{18,19} Further refinements based on advanced charge transport descriptions and unintentional doping effects have precisely described the thickness-dependent photocurrent.²⁰

Despite acutely affecting the OPV performance,^{21–25} predicting the optimum D:A ratio has been much more challenging due

to the complexity of charge photogeneration and transport through the blend towards the electrodes. For semicrystalline polymers blended with fullerenes, optimum D:A ratios have been rationalized by the binary phase diagram.²¹ In particular, slightly hypoeutectic concentrations with respect to the polymer loading were found to lead to a good compromise between charge generation and appropriate percolating pathways for charges to reach the electrodes. Also the balance of charge carrier mobilities between electrons and holes has often been considered a key feature determining the shape of the photocurrent–composition curve²⁶ (hereafter referred to as J_{sc} -vol%). The current OPV paradigm led by NFAs as excellent light harvesters adds another ingredient to the J_{sc} -vol% dependence compared to fullerene-based devices since photocurrent generation is now fully distributed between both materials. Given the intricate optoelectronic trade-off that sets the location of the optimum D:A ratio, novel experimental approaches and data-driven predictive models are required to enhance the current understanding of the J_{sc} -vol% dependence in binary OPV blends.

In this work, we adopt a synergic combination of experimental high-throughput screening and AI to study the relationship between the photocurrent generation and the active layer parameters (*i.e.* thickness and D:A ratio) in binary OPV devices. The experimental exploration is performed by processing orthogonal parametric gradients or libraries, which in combination

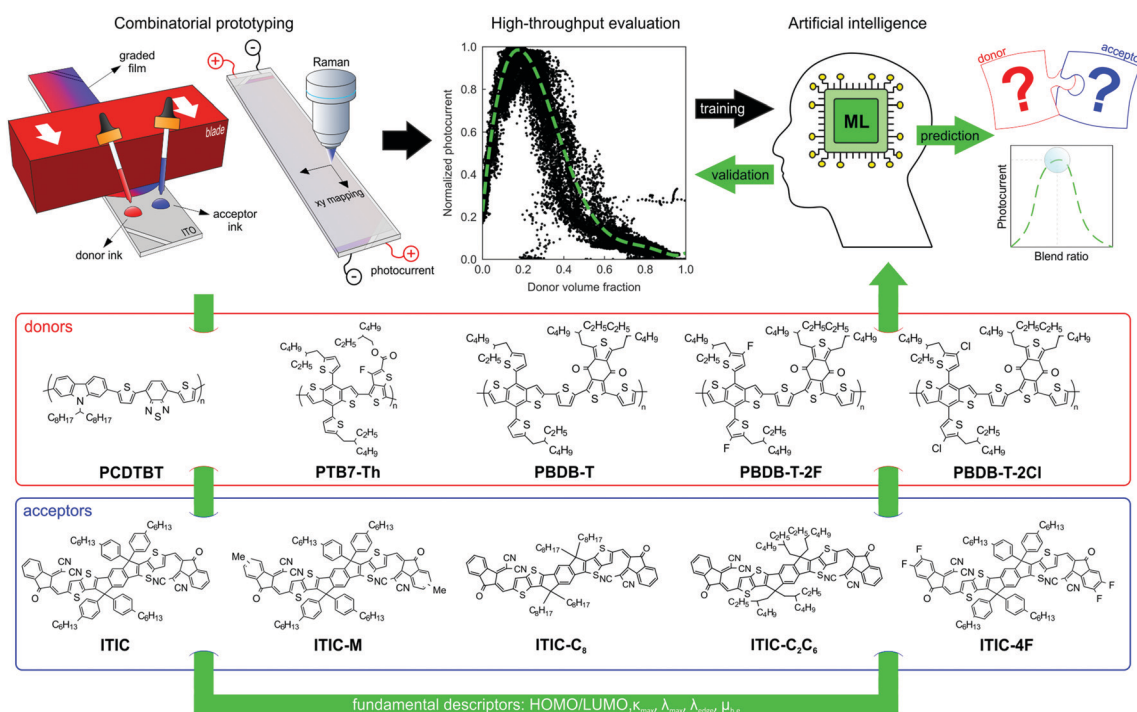


Fig. 1 The photocurrent–composition prediction workflow for binary OPV blends is divided into three main blocks. First, the generation of parametric libraries by blade coating on functional devices in the form of lateral gradients in the active layer thickness and the D:A ratio. Second, the high-throughput photovoltaic characterization by means of co-local Raman spectroscopy and photocurrent imaging, which serves to correlate the local device performance with the variation of the target features (thickness and D:A ratio). Third, AI algorithms are trained on the experimental datasets using intrinsic fundamental descriptors of the blended materials. In the last step, the AI models are exploited to make predictions of the photocurrent–composition dependence for materials in and outside of the training dataset.



with local probing techniques (namely Raman spectroscopy and photocurrent imaging) serve to assess the corresponding photocurrent phase space diagrams with minimal effort.^{27–32} The exploration results in a plethora of possible J_{sc} -vol% dependences: from strongly skewed bell shapes to bimodal distributions. Then, in an attempt to rationalize these complex relationships, we implement two different AI algorithms that take as input a series of intrinsic optoelectronic material descriptors. The first algorithm is a Bayesian machine scientist,³³ which is found to complement the high-throughput experimental screening due to its large descriptive power while providing an analytical equation to describe the intricate J_{sc} -vol% phase spaces. Second, we use a random forest (RF) algorithm as a predictive model for the normalized J_{sc} -vol% dependences retrieving a mean absolute error (MAE) below 0.20 in untrained OPV binaries. In the RF models, we find that descriptors related with the alignment of the frontier energy levels and the mobility difference are statistically relevant in shaping the J_{sc} -vol% space. Finally, feature selection procedures reveal highly predictive models when only the donor and acceptor electronic (or optical) band gaps are employed in the training step. The RF models found herein define the J_{sc} -vol% curves in both NFA and fullerene-based binary blends with excellent accuracy.

Results

General workflow

Fig. 1 illustrates the high-throughput evaluation, training, and prediction workflow used throughout the article. The processing of compositional libraries was accomplished by blade coating *via* the coalescence of pristine donor and acceptor ink drops at the blade reservoir. The blade movement induced their mixing during the coating to generate a compositional gradient perpendicularly to the displacement direction.²⁹ In parallel, ink depletion at the front reservoir generates a thickness gradient along the blade movement direction. The dissimilar ink rheology also created film thickness fluctuations in conjunction with the D:A ratio library (see Section I in the ESI†). Following electrode deposition, a simultaneous characterization based on Raman spectroscopy and light-beam induced-current (LBIC) mapping was used to image the heterogeneous film features including thickness and composition,³⁴ and to correlate them to the corresponding photocurrent images. This approach allowed the efficient exploration of the photocurrent phase diagram of binary OPV blends in a combinatorial manner: the time and semiconductor material cost requirements can be as low as 90 seconds and 50 ng per data point, respectively (see Section II in the ESI†).

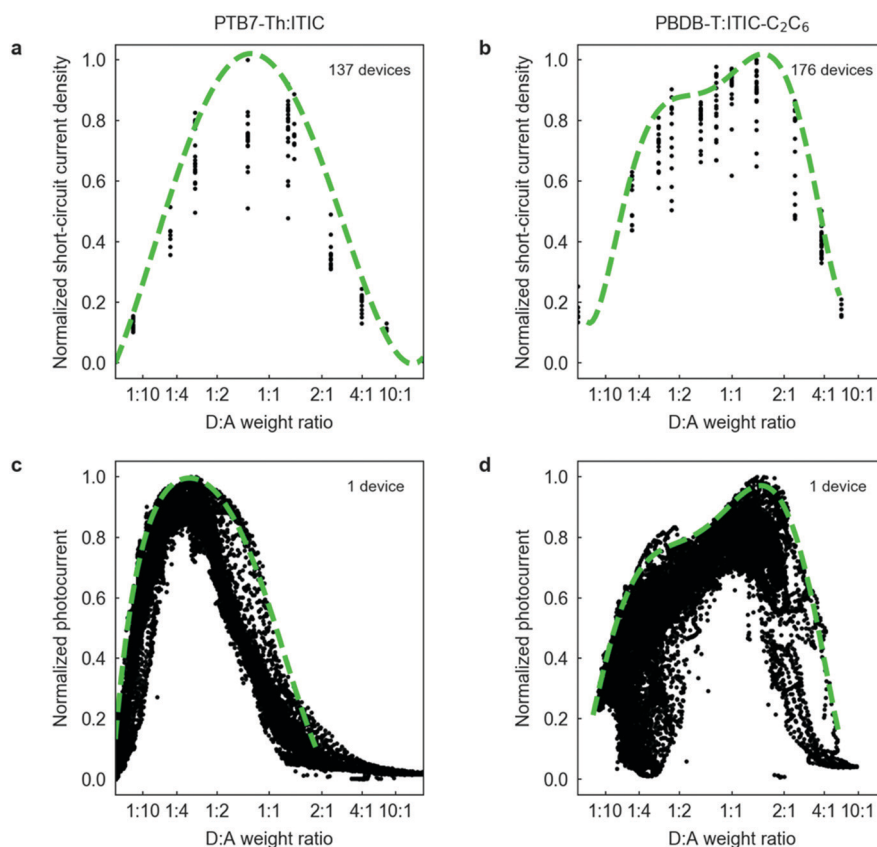


Fig. 2 (a and b) Normalized distribution of the short-circuit current density obtained in discrete devices as a function of the D:A weight ratio in PTB7-Th:ITIC and PBDB-T:ITIC-C₆₀ blends. (c and d) Normalized photocurrent dispersion obtained following the high-throughput optimization approach for the same blends. Green dashed lines are polynomial fits of the high-performing envelope of photocurrent values. In each case we indicate the number of devices needed to generate these plots. The reader is referred to Section I in the ESI† for further details on device manufacture.



The highly efficient screening process generated large amounts of thickness–composition parametric combinations per D:A pair in the corresponding J_{sc} space (*ca.* 24 000 data points). This was then employed in the training and validation of AI algorithms together with fundamental optoelectronic material descriptors such as highest occupied molecular orbital (HOMO) and lowest unoccupied molecular orbital (LUMO) energy levels, absorption coefficients (see Section III in the ESI†) and charge carrier mobilities. As detailed in Section IV in the ESI†, the descriptors extracted from literature can be selected following distinct criteria. With these data, we first validated the ability of the AI models to reconstruct the complete J_{sc} –vol% diagram and then predict the corresponding dependence for material combinations out of the original training set. This approach is exploited to determine the optimum active layer thickness and composition in terms of photocurrent for any D:A pair (with known input descriptors).

High-throughput experimental screening

Herein, the high-throughput experimentation strategy based on lateral parametric libraries substitutes the traditional sample-by-sample methodologies (*aka* Edisonian experimentation) in the screening of the J_{sc} –vol% space. Hence, we first verify that both approaches converge to the same figures in the normalized J_{sc} –vol% diagram. Fig. 2 compares the J_{sc} dispersion obtained following the traditional fabrication-intensive protocol (Fig. 2a and b) and the measuring-intensive strategy proposed here (Fig. 2c and d). We study two high-performing OPV binary systems, namely the workhorse PTB7-Th:ITIC blend³⁵ as well as a novel, unreported binary formed by PBDB-T:ITIC–C₆₀. The preparation of premixed inks from pristine D and A aliquots (as required in traditional experimentation procedures) enables us to estimate the corresponding D:A density ratios, ξ (see Section VII in the ESI†). In Fig. 2 we accordingly transform vol% to the more familiar D:A weight ratio typically followed in OPV sample preparation. However, the transformation from vol% to wt% does not generally lead to an acute displacement of the scattered data distributions since ξ is found to be close to unity in the here explored cases. This indicates that J_{sc} –vol% phase diagrams (as raw-extracted from optical probes such as Raman or ellipsometry) will generally resemble quite closely J_{sc} –wt% distributions. On the other hand, the observed photocurrent dispersion along the y-axis in Fig. 2a and b is mainly related to the screening of the active layer thickness as we varied the thickness at each composition in the pursuit of the optimum thickness at each blending ratio (see Section I in the ESI†). Importantly, the two systems exhibit very different J_{sc} –wt% curves, one being a single peak centered at *ca.* 40 wt% of donor, while the other appears bimodal (*vide infra*).

Notably, the high-throughput methodology reproduces the unimodal and bimodal photocurrent dispersions observed as a function of the donor loading in both binaries (Fig. 2c and d). Importantly, it does so with very large statistics, strongly reducing the uncertainty with respect to the actual shape of the curve. In this approach, the vertical J_{sc} dispersion originates from both active layer thickness and morphology variations, the latter being a consequence of the *in situ* mixing of the

pristine inks in the blade reservoir. By quantifying the Raman blue-shifting of the corresponding D and A vibrational fingerprints, we have verified that devices containing compositional gradients can reproduce the degree of mixing attained when casting fully premixed solutions. Moreover, they embrace a richer catalogue of film morphologies than conventional methodologies expanding the available data to correlate microstructure and device performance (see Section II in the ESI†). Note that the high-throughput screening requires a significantly reduced amount of experimental time and resources: hundreds of discrete devices (here 137 and 176 devices in PTB7-Th:ITIC and PBDB-T:ITIC–C₆₀, respectively) *versus* a single combinatorial device per binary.

The high-throughput methodology has, however, the caveat of measuring J_{sc} only rather than the full set of solar cell parameters (open-circuit voltage (V_{oc}), fill factor (FF) and PCE). Nevertheless, since V_{oc} remains fairly constant, the PCE correlates well with J_{sc} for the range of compositions of interest despite the variations observed in FF (see Section II in the ESI†), which is in excellent agreement with the overall trends depicted from data-mining studies (*i.e.* J_{sc} is the best proxy for PCE).¹⁷ Interestingly, we have determined that parameters related with morphology such as Raman (blue)-shifting and photoluminescence (PL) quenching and shifting are closely related with microstructure and FF, thus opening up the possibility to take into account their effect in the high-throughput determination of the D:A ratio that maximizes the overall PCE (see Section II in the ESI†). On the other hand, the use of non-standardized white light for the acquisition of the J_{sc} data (see Section I in the ESI†) and the intrinsic uncertainty of the Raman-based determination of composition³⁴ can explain the small differences observed in the photocurrent distributions when comparing both optimization protocols; more specifically, the *ca.* 15 wt% offset in the donor content that maximizes the photocurrent in PTB7-Th:ITIC devices. Nonetheless, these drawbacks are significantly outweighed by the rapid attainment of large experimental datasets, which serve as ideal seeds for training AI algorithms. Furthermore, the experimental approach demonstrates high reproducibility from batch-to-batch (see Section II in the ESI†).

Implementation of artificial intelligence algorithms

We next examine the upper crust of the scattered photocurrent distribution observed in the combinatorial samples (dashed green lines in Fig. 2c and d). These provide a large overview of the photocurrent phase space in a very efficient manner. After determining the optical properties of the D:A blends (see Section III in the ESI†) and indexing their electronic properties from the literature (see attached spreadsheet in the ESI†), we start feeding AI algorithms to elucidate the origin of the observed trends. Our tentative list of relevant descriptors contains 23 elements per D:A pair, including eight dimensionless parameters (see Section IV in the ESI†). At this stage, we did not include descriptors based on properties of the blends, such as their phase diagrams.



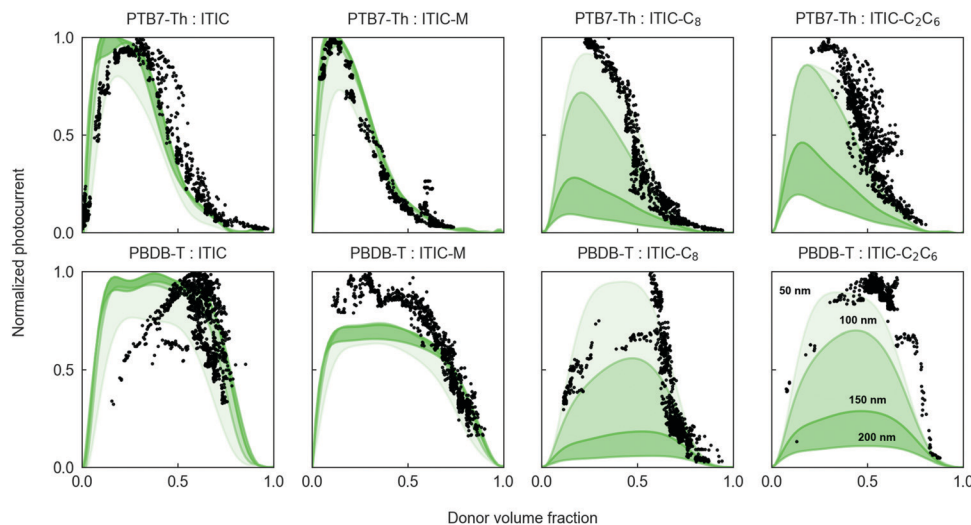


Fig. 3 A Bayesian machine scientist successfully models the photocurrent phase space in OPV binaries. The high-throughput experimental evaluation approach is first exploited to efficiently explore the corresponding photocurrent phase space as a function of the active layer thickness and the D : A ratio. Then, 1000 high-performing photocurrent data points obtained in each of the eight different D:A combinations of PTB7-Th (upper row) and PBDB-T (lower row) blended with ITIC, ITIC-M, ITIC-C₈ and ITIC-C₂C₆, are selected to train a Bayesian machine scientist. The training results in a unified model equation including eight dimensionless parameters that can fully explore the photocurrent phase space. Such an equation enables evaluation of tolerances upon thickness and D : A ratio fluctuations as illustrated by the solid green curves and shaded areas, which delimit the high-performing shell of normalized photocurrent values at distinct active layer thicknesses: 200 nm, 150 nm, 100 nm and 50 nm.

Our first implementation of AI is a Bayesian machine scientist,³³ which includes the dimensionless descriptors as inputs to develop analytical models that explore the J_{sc} -vol% dependence (see Section V in the ESI[†]). For any given set of scattered data, the Bayesian machine scientist identifies the plausible and simplest mathematical models that describe the observed trends. We applied this methodology to two families of OPV binaries (Fig. 3) with PTB7-Th and PBDB-T as donors, individually blended with four ITIC-based acceptors showing either distinct end groups (ITIC-M) or side-chains (ITIC-C₈ and ITIC-C₂C₆). We note that, experimentally, small but non-zero photocurrent has been measured for some pristine NFAs. A full study of this goes beyond the scope of this manuscript, but it is worth noting it, even when the corresponding solar cells have comparatively low overall efficiencies.

According to the solid curves in Fig. 3, which delimit the J_{sc} -vol% space encountered at different active layer thickness values, the Bayesian machine scientist reproduces well the highest-performing experimental trends. The actual model equation is provided in Section V in the ESI[†]. While we would not rationalize any physical meaning, we use it to evaluate the parameter space. Importantly, regarding the photocurrent phase space, the modeling indicates that (i) PTB7-Th binaries are characterized by sharp and unbalanced compositional optimum peaks; (ii) PBDB-T blends are more tolerant to compositional fluctuations and their maxima are more balanced in D:A ratio; (iii) binaries containing ITIC and ITIC-M show limited thickness dependence; (iv) ITIC-C₈ and ITIC-C₂C₆ blends are very sensitive to active layer thickness variations; and (v) the bimodal distribution is more or less pronounced depending on the actual thickness range. Despite the great descriptive power of the machine scientist in completing the

exploration of the complex photocurrent phase space, it has some limitations arising from its computational complexity and the size of the training dataset, including: (i) month-scale times needed for training; (ii) poor predictive capability out of the training materials dataset due to the unfeasibility of sampling models for long enough time; and (iii) an uninformative utilization of the features, which makes it impossible to determine which of them are really important.

Therefore, we tested alternative ML approaches such as the random forest (RF) algorithm to improve the predictive capability of the AI models. The RF ensemble is initially trained using the same OPV binaries previously explored by the Bayesian machine scientist, which are highlighted with green frames in Fig. 4. The validation (testing) datasets are highlighted in blue while the purely predictive scenarios are framed in magenta color. Thus, Fig. 4 accordingly depicts a combinatorial matrix of the scattered J_{sc} -vol% dependences obtained in distinct D:A pairs following the high-throughput experimentation approach, as well as the RF model predictions (dashed lines) at different active layer thickness values (colored from grey to black). Therein, we include organic semiconductors out of the pristine training material set such as PCDTBT as donor polymer and two additional acceptors, namely a fluorinated ITIC derivative (ITIC-4F) and the workhorse fullerene, PC₇₀BM.

As part of the RF model validation process, we first perform a leave-one-out cross-validation (LOO-cv) of the RF ensemble including the 8 training datasets (green frames in Fig. 4), as detailed in Section VI in the ESI[†]. Based on the extrapolation reliability found (*ca.* 65% of success rate), we further validated the RF model by comparing the predicted trends with the experimental results obtained in D:A pairs out of the training set selection, *i.e.* binaries for which either one or the two



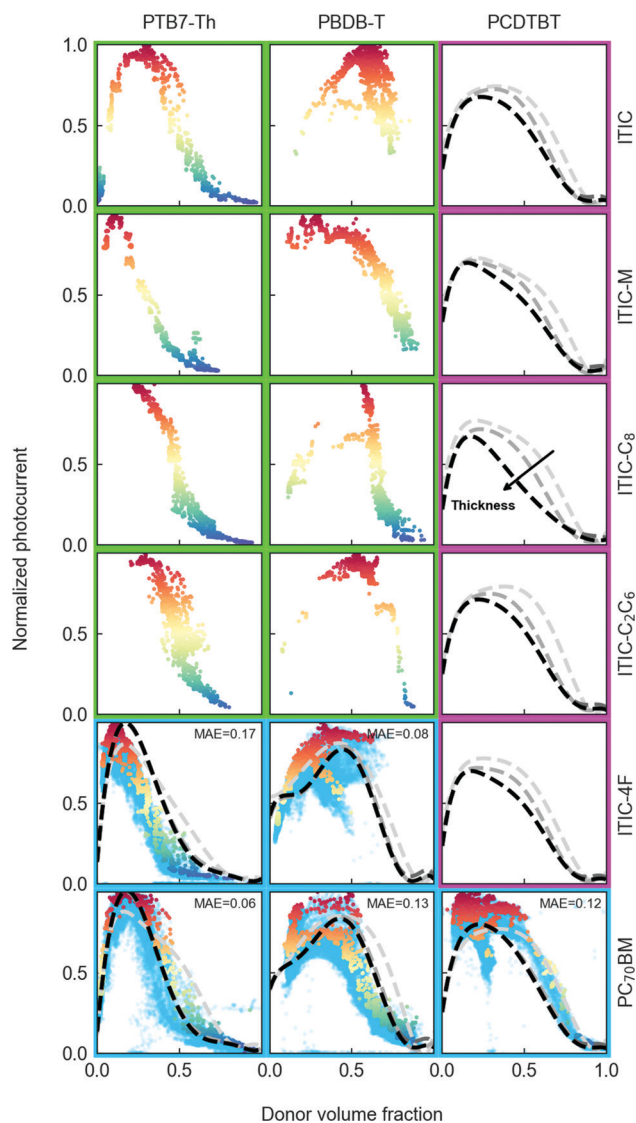


Fig. 4 Combinatorial matrix of photocurrent phase diagrams for a set of high-performing polymer donors (PTB7-Th and PBDB-T) and acceptors, including traditional fullerenes (PC₇₀BM) as well as a family of novel NFAs (ITIC and its derivatives: ITIC-M, ITIC-C₈, ITIC-C₂C₆ and ITIC-4F). The photovoltaic performance is assessed by quantifying the photocurrent under white light illumination (y-axis) as a function of the donor polymer loading (x-axis) and the active layer thickness (whose dependence is implicit in the y-axis dispersion). Datasets are highlighted in green (training), blue (validation) and magenta (prediction) in correspondence with the type of D:A combinations when in use with random forest (RF) models. The mean absolute error (MAE) of the RF model in reproducing the photocurrent upper shell of 1000 values (depicted in colored rainbow scale, to be distinguished from the remaining experimental data points in blue) is shown for the validation datasets. The dashed lines correspond to the RF model predictions obtained at different active layer thickness values: from 50 nm (lightest grey) to 200 nm (black).

materials have not been used within the training step (blue frames in Fig. 4). This trait is precisely the main feature desired for highly predictive models.

Our results indicate that the RF model extrapolates very well (MAE < 0.20) in all validation binaries explored, both the position of the J_{sc} maximum and its modulation in the

composition (and thickness) diagram. The results obtained are equally consistent when validating a larger combinatorial matrix including data for high performing donor polymers such as PBDB-T-2Cl (PM7) and PBDB-T-2F (PM6), see Fig. S23 in the ESI.† It is worth highlighting that regardless of the molecular nature of the materials blended, the only model inputs for the extrapolation are the corresponding optoelectronic descriptors used in the training of the RF algorithm. In this particular case, we hand-picked the HOMO/LUMO energy levels reported from cyclic voltammetry (CV) measurements only as well as the corresponding mobilities from the same references (whenever possible), as detailed in Section IV in the ESI.†

Discussion

Undoubtedly, the predictive power of the RF model is remarkable given its simplicity. From a chemical and fundamental point of view, the dissimilarities between the materials employed in the training and both PCDTBT and PC₇₀BM (as the most distinct validation species in Fig. 4) are important. The type of moieties in the backbone and grafted side chains (for the donor polymers), as well as the chemical structure and topology (for the acceptors) are significantly different. Despite these acute differences, the RF model draws well the J_{sc} -vol% dependence experimentally found in the validation datasets. On the other hand, the predictive capability of the RF model (magenta panels in Fig. 4) is extremely powerful to evaluate *a priori* the J_{sc} -vol% diagram of any OPV binary, including their tolerance against blending ratio fluctuations. This latter fact has important consequences in the upscaling of any novel D:A pair and is largely acknowledged in the OPV industry. Indeed, our results are very promising considering the limited number (8) of D:A material combinations employed in our first tentative model training. Further enhancements in the predictive power can be expected when the training set is extended or additional material-specific descriptors are included, such as the molecular structures.

AI models, such as the RF ensemble, also provide the so-called feature importance (FI), a magnitude that serves to identify and rank quantitatively those characteristics that mostly govern the experimental observables, *i.e.* the J_{sc} -vol% dependence. Accordingly, we first perform subsequent FI analysis using three distinct selections of optoelectronic descriptors. These differ on how the actual values are picked from the literature database (> 80 references accessed): either randomly, by a consistent manual selection or calculated from the statistical medians of the scattered data. This analysis is performed to evaluate the sensitivity of the model against the consistency of the input descriptors. The accumulated analysis of the FI in each model (Fig. 5) indicates that parameters related to the HOMO/LUMO energy level alignment, such as CT_e , CT_h or $E_{gap,d-a}$, as well as those related to the mobility of the blended species ($\Delta\mu$ and μ_{imb}) are, statistically, the most important descriptors in defining the J_{sc} -vol% dependence. These findings are in good agreement with the current



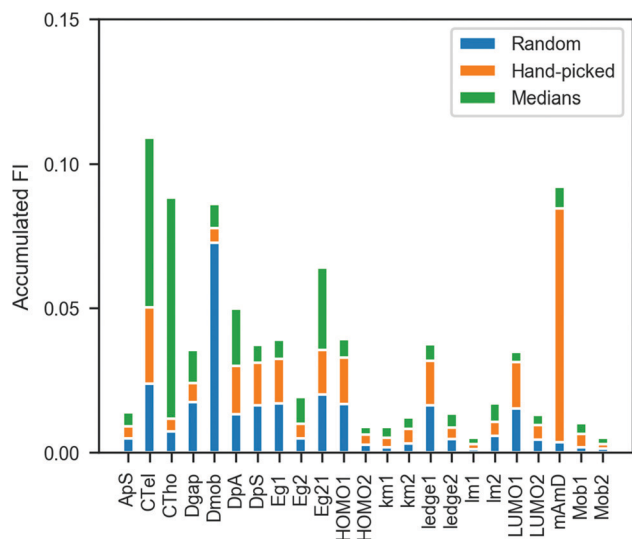


Fig. 5 Accumulated feature importance (FI) depending on the choice of descriptor values. Since the HOMO and LUMO energy levels as well as the charge carrier mobilities are taken from the literature, we explore the effect that the actual value of the descriptors has on the FI drawn by the RF ensemble. We generally observe that descriptors related with energy level alignment (CT_{el} , CT_{th} , $E_{\text{gap,d-a}}$) as well as those related with the mobility imbalance ($\Delta\mu = |\mu_{\text{d}} - \mu_{\text{a}}|$, $\mu_{\text{imb}} = \mu_{\text{a}}/\mu_{\text{d}}$) show the highest accumulated FI. The reader is referred to Section IV in the ESI† for a detailed mathematical definition of the descriptors employed.

understanding of the performance–composition space in OPV, as the existence of unbalanced charge carrier mobility has been considered one of the key features that influences the J_{sc} –vol% diagram in binary blends.²⁶ Nevertheless, we observe that the

actual selection of values for the descriptors has a large effect on the FI distribution, thus highlighting the requirement for great consistency among the experimental data selected or measured. In this regard, feature selection approaches might help in identifying those combinations of descriptors that return more robust models against experimental noise.

In particular, by performing a greedy MAE feature selection procedure we identify several two-parameter combinations that yield highly accurate RF models, even showing in some cases lower MAE than those models trained with a larger list of descriptors (see Section VI in the ESI†). Among them, we would like to highlight the pair formed by $E_{\text{gap,d}}$ and $E_{\text{gap,a}}$, whose LOO-cv in 15 distinct D:A binaries is depicted in Fig. 6. This model, based on $E_{\text{gap,s}}$, is remarkably robust against experimental fluctuations and it extrapolates moderately well in some unseen blends, including all-polymer binaries (see Section VI in the ESI†). Moreover, successful model equations are drawn by the Bayesian machine scientist when employing these two descriptors only (see Section V in the ESI†). Finally, we observe that model training using the consistently extracted solid-state optical band gaps from Tauc plots results as well in successfully validated RF models (see Section VI in the ESI†). Hence, $E_{\text{gap,d}}$ and $E_{\text{gap,a}}$ (either electronic or optical) unify the main learning characteristics previously found by the 23-parameter model yet in a more physically intuitive approach and providing comparable predictive accuracy. Nevertheless, model predictions in workhorse D:A pairs such as P3HT:PC₆₀BM are not successful, which we believe is a consequence of the limited extension of the training datasets employed and the absence of highly semi-crystalline donor polymers in our training dataset.

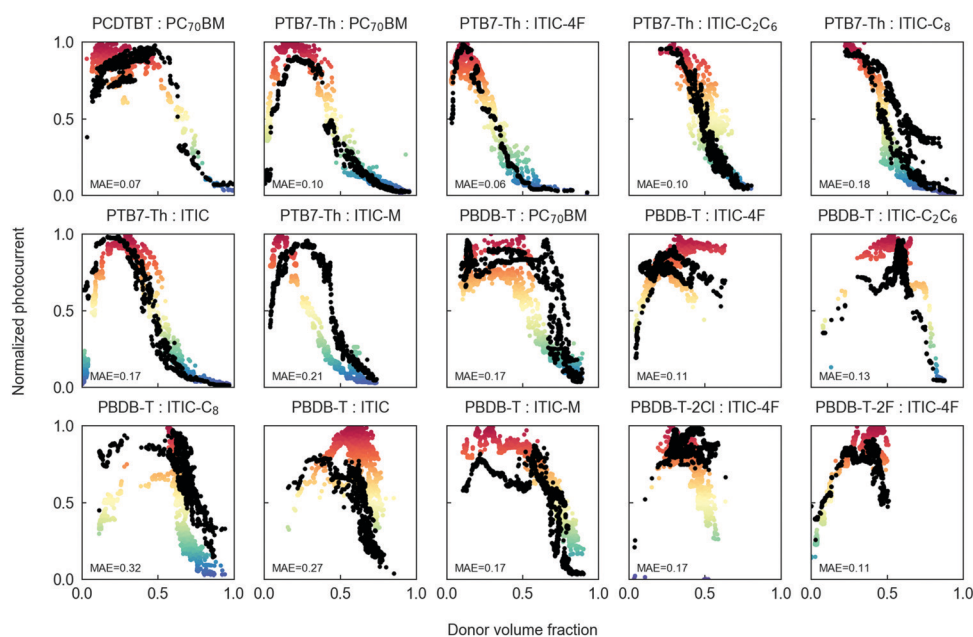


Fig. 6 Leave-one-out cross-validation (LOO-cv) of the two-parameter random forest (RF) model. By performing a greedy mean absolute error (G-MAE) feature selection procedure we identify the corresponding donor and acceptor electronic band gaps ($E_{\text{gap,d}}$ and $E_{\text{gap,a}}$) as one of the most descriptive paired features in two-parameter RF models. The corresponding LOO-cv predictions (black dots) performed in 15 experimental datasets show excellent agreement with the experimental normalized J_{sc} distributions (rainbow colored), with a MAE of 0.16 (± 0.07). The RF models are evaluated at the same grid of thickness–composition values as the experimental measurements.



In spite of such limitations, we believe that the simplicity and accuracy of this two-parameter model are powerful for several reasons: (i) for theoretical material screening, as E_{gap} is a byproduct of density functional theory (DFT) calculations; (ii) for combinatorial material synthesis, as organic semiconductors are usually subjected to CV to quantify the HOMO–LUMO energy levels as part of a routine set of electrochemical characterizations; and (iii) because E_{gap} is a magnitude sufficiently unrelated to processing. We further note that similar predictive accuracy can be obtained by using easily measured solid-state optical band gaps in the model training.

These features are especially advantageous when dealing with small batches of novel materials. In this case, RF models may help researchers to tailor more effectively the optimal device features (*i.e.* active layer thickness and composition) and explore *de facto* the full photovoltaic potential of the new molecular species. The here employed training dataset initially formed by 15 D:A binaries is in constant growth; therefore, the conclusions extracted by the RF model will be progressively refined blend after blend. For this reason, we make accessible our combinatorial screening database in a public CSIC repository (<http://hdl.handle.net/10261/223231>), which is open to contributions from any researchers as part of a joint OPV materials screening project.

Conclusions

In this work, we have shown the synergic use of high-throughput experimentation and AI algorithms for the prediction of the J_{sc} –vol% space in binary bulk heterojunction organic solar cells. The generation of combinatorial libraries *via* blade coating and their subsequent imaging by Raman spectroscopy and LBIC mapping enables the efficient exploration of the complex performance landscape in such devices. The subsequent training of a Bayesian machine scientist is demonstrated to be useful in filling the corresponding parameter space, which serves to evaluate the sensitivity of the selected binary upon variations of composition, active layer thickness and other intrinsic optoelectronic descriptors. We finally validate RF models that are able to predict the J_{sc} –vol% dependence with excellent accuracy in unseen binary blends (*i.e.* blends that are not in the training materials set). We identify descriptors related with the HOMO/LUMO energy level alignment of the donor and acceptor materials, as well as their mobility imbalance among the most important features in shaping the J_{sc} –vol% predictions. Interestingly, simple intuitive models of only two features, namely the electronic (or solid-state optical) band gaps of the blended species, reproduce with large accuracy the J_{sc} –vol% dependence.

Conflicts of interest

The authors declare no competing interests.

Acknowledgements

This work was supported by the Spanish Ministerio de Ciencia e Innovación under Grants PGC2018-095411-B-I00, FIS2016-78904-C3-1-P, and SEV-2015-0496 in the framework of the Spanish Severo Ochoa Centre of Excellence. We acknowledge financial support from the European Research Council through project ERC CoG 648901 and the H2020 Marie Curie actions through the SEPOMO project (grant number 722651). X. R.-M., E. P.-S.-J. and M. C.-Q. thank Dr Bernhard Dörfling for designing the doctor blade controller and Mr Martí Gibert-Roca for designing the multiplexer/switcher. X. R.-M. acknowledges the departments of Physics, Chemistry and Geology of the Autonomous University of Barcelona (UAB) as coordinators of the PhD program in Materials Science. M. H. acknowledges the Royal Society and the Wolfson Foundation. The authors thank Dr Mathieu Linares and Dr Jasper Michels for inspiring discussions at the early stages of this work. We acknowledge support of the publication fee by the CSIC Open Access Publication Support Initiative through its Unit of Information Resources for Research (URICI).

References

- 1 O. Inganäs, *Adv. Mater.*, 2018, **30**, 1800388.
- 2 C. Yan, S. Barlow, Z. Wang, H. Yan, A. K.-Y. Jen, S. R. Marder and X. Zhan, *Nat. Rev. Mater.*, 2018, **3**, 18003.
- 3 P. Cheng, G. Li, X. Zhan and Y. Yang, *Nat. Photonics*, 2018, **12**, 131–142.
- 4 J. Hou, O. Inganäs, R. H. Friend and F. Gao, *Nat. Mater.*, 2018, **17**, 119–128.
- 5 G. Li, W.-H. Chang and Y. Yang, *Nat. Rev. Mater.*, 2017, **2**, 17043.
- 6 C. Liu, K. Wang, X. Gong and A. J. Heeger, *Chem. Soc. Rev.*, 2016, **45**, 4825–4846.
- 7 Q. Liu, Y. Jiang, K. Jin, J. Qin, J. Xu, W. Li, J. Xiong, J. Liu, Z. Xiao, K. Sun, S. Yang, X. Zhang and L. Ding, *Sci. Bull.*, 2020, **65**, 272–275.
- 8 K. Vandewal, K. Tvingstedt, A. Gadisa, O. Inganäs and J. V. Manca, *Phys. Rev. B: Condens. Matter Mater. Phys.*, 2010, **81**, 125204.
- 9 K. Vandewal, K. Tvingstedt, A. Gadisa, O. Inganäs and J. V. Manca, *Nat. Mater.*, 2009, **8**, 904–909.
- 10 V. D. Mihailetschi, H. X. Xie, B. de Boer, L. J. A. Koster and P. W. M. Blom, *Adv. Funct. Mater.*, 2006, **16**, 699–708.
- 11 J. Hachmann, R. Olivares-Amaya, S. Atahan-Evrenk, C. Amador-Bedolla, R. S. Sánchez-Carrera, A. Gold-Parker, L. Vogt, A. M. Brockway and A. Aspuru-Guzik, *J. Phys. Chem. Lett.*, 2011, **2**, 2241–2251.
- 12 H. Sahu, W. Rao, A. Troisi and H. Ma, *Adv. Energy Mater.*, 2018, **8**, 1801032.
- 13 H. Sahu, F. Yang, X. Ye, J. Ma, W. Fang and H. Ma, *J. Mater. Chem. A*, 2019, **7**, 17480–17488.
- 14 S. A. Lopez, B. Sanchez-Lengeling, J. de Goes Soares and A. Aspuru-Guzik, *Joule*, 2017, **1**, 857–870.
- 15 W. Sun, Y. Zheng, K. Yang, Q. Zhang, A. A. Shah, Z. Wu, Y. Sun, L. Feng, D. Chen, Z. Xiao, S. Lu, Y. Li and K. Sun, *Sci. Adv.*, 2019, **5**, eaay4275.



- 16 H. Sahu and H. Ma, *J. Phys. Chem. Lett.*, 2019, **10**, 7277–7284.
- 17 S. Nagasawa, E. Al-Naamani and A. Saeki, *J. Phys. Chem. Lett.*, 2018, **9**, 2639–2646.
- 18 L. A. A. Pettersson, L. S. Roman and O. Inganäs, *J. Appl. Phys.*, 1999, **86**, 487.
- 19 D. W. Sievers, V. Shrotriya and Y. Yang, *J. Appl. Phys.*, 2006, **100**, 114509.
- 20 F. Deledalle, T. Kirchartz, M. S. Vezie, M. Campoy-Quiles, P. Shakya Tuladhar, J. Nelson and J. R. Durrant, *Phys. Rev. X*, 2015, **5**, 011032.
- 21 C. Müller, T. A. M. Ferenczi, M. Campoy-Quiles, J. M. Frost, D. D. C. Bradley, P. Smith, N. Stingelin-Stutzmann and J. Nelson, *Adv. Mater.*, 2008, **20**, 3510–3515.
- 22 P. Wolfer, P. E. Schwenn, A. K. Pandey, Y. Fang, N. Stingelin, P. L. Burn and P. Meredith, *J. Mater. Chem. A*, 2013, **1**, 5989.
- 23 Y. Zhang, Y. Xu, M. J. Ford, F. Li, J. Sun, X. Ling, Y. Wang, J. Gu, J. Yuan and W. Ma, *Adv. Energy Mater.*, 2018, **8**, 1800029.
- 24 Z. Wen, X. Ma, X. Yang, P. Bi, M. Niu, K. Zhang, L. Feng and X. Hao, *Chin. Chem. Lett.*, 2019, **30**, 995–999.
- 25 S. S. van Bavel, M. Bärenklau, G. de With, H. Hoppe and J. Loos, *Adv. Funct. Mater.*, 2010, **20**, 1458–1463.
- 26 Y. Firdaus, V. M. Le Corre, J. I. Khan, Z. Kan, F. Laquai, P. M. Beaujuge and T. D. Anthopoulos, *Adv. Sci.*, 2019, **6**, 1802028.
- 27 M. Kiy, R. Kern, T. A. Beierlein and C. J. Winnemisser, *Organic Light Emitting Materials and Devices X*, 2006, vol. 6333, p. 633307.
- 28 S. Langner, F. Häse, J. D. Perea, T. Stubhan, J. Hauch, L. M. Roch, T. Heumueller, A. Aspuru-Guzik and C. J. Brabec, *Adv. Mater.*, 2020, **32**, 1907801.
- 29 A. Sánchez-Díaz, X. Rodríguez-Martínez, L. Córcoles-Guija, G. Mora-Martín and M. Campoy-Quiles, *Adv. Electron. Mater.*, 2018, **4**, 1700477.
- 30 A. Harillo-Baños, X. Rodríguez-Martínez and M. Campoy-Quiles, *Adv. Energy Mater.*, 2020, **10**, 1902417.
- 31 K. Glaser, P. Beu, D. Bahro, C. Sprau, A. Pütz and A. Colmann, *J. Mater. Chem. A*, 2018, **6**, 9257–9263.
- 32 E. Pascual-San-José, X. Rodríguez-Martínez, R. Adel-Abdelaleim, M. Stella, E. Martínez-Ferrero and M. Campoy-Quiles, *J. Mater. Chem. A*, 2019, **7**, 20369–20382.
- 33 R. Guimerà, I. Reichardt, A. Aguilar-Mogas, F. A. Massucci, M. Miranda, J. Pallarès and M. Sales-Pardo, *Sci. Adv.*, 2020, **6**, eaav6971.
- 34 X. Rodríguez-Martínez, M. S. Vezie, X. Shi, I. McCulloch, J. Nelson, A. R. Goñi and M. Campoy-Quiles, *J. Mater. Chem. C*, 2017, **5**, 7270–7282.
- 35 Y. Lin, J. Wang, Z.-G. Zhang, H. Bai, Y. Li, D. Zhu and X. Zhan, *Adv. Mater.*, 2015, **27**, 1170–1174.

